JOURNAL OF AIRCRAFT
Vol. 46, No. 2, March–April 2009

New Electric Field Computation Method for Aircraft

Xingya Da,* Huairong Shen,† and Lei Hong‡
Academy of Equipment Command and Technology, 101416 Beijing , People's Republic of China

DOI: 10.2514/1.38699

This paper presents a new electric field computation method for aircraft to solve the problems caused by corona emissions. At the core of this new method is the use of the method of moments, the right and left symmetrical meshing that decreases a half-patch. The new method also employs a solution for large linear systems based on the eigenvalue decomposition that resolves the stagnation problems of large nonsymmetrical matrices with large condition numbers. Using the method of moments establishes the distorted field computation model of only the aircraft net charge and the ambient field around the aircraft. This, in turn, makes it more convenient to apply the proposed method. Simulations on a real unmanned aerial vehicle are also made to validate this method and analyze the main corona-emission trigger factor. The results show that the new method could guarantee speed and precision compared with the previous methods, indicating that corona emissions are mainly triggered by the aircraft net charge. A scheme is proposed to predict the corona emissions for atmospheric electric field measurement aircraft using the new method.

I. Introduction

CORONA emissions not only endanger an aircraft's safety, they also affect aeroexploration applications. For instance, taking the atmospheric electric field measurement in an aircraft, the error caused by corona emissions could run up to dozens of kilovolts per meter [1]. To improve measurement precision, it is necessary for explorers to accurately identify when and where corona ions are emitted from the aircraft and how they affect the measurements; this is also important for other applications.

The present aircraft corona studies have mostly been completed by analyzing the spectrum data and some electric field measurements [1–3]. However, these still cannot precisely explain when and where corona ions are emitted from the aircraft, due to the complex ambient environment and aircraft surface. This deficiency and the need to understand corona emissions motivated us recently to compute the electric field around an aircraft. The corona is triggered by the extremely distorted field distributions around the corona point brought about by the aircraft net charge and the strong atmospheric electric field. Thus, the computation of the electric field can help us predict corona emissions and model the corona current. However, it is rather difficult to do so, despite the fact that many methods have been developed to compute it, including the finite difference methods [4,5], the charge simulation methods [6], and the method of moments [7,8].

Knowing that the fields around an aircraft are linear with the aircraft net charge and the ambient field, a recent attempt was made by Da et al. [9] to compute the fields around an aircraft. Although their method is based on the method of moments, they creatively established the computation model for $\boldsymbol{C}$, which they used to compute a field through $\boldsymbol{E} = \boldsymbol{C}[E_x\ E_y\ E_z\ Q]^T$, where E_x, E_y, and E_z represented the atmospheric field components in an aircraft body frame and Q represented the aircraft net charge. Compared with the previous methods, field computation thus became more convenient after the introduction of $\boldsymbol{C}$. Da et al. also studied the numeric computation method for $\boldsymbol{C}$ and analyzed the main corona trigger factor using an ellipsoid as a simplified fuselage model. The simulation results showed that their findings were precise and applicable. However, there is one shortage that must be paid attention to, and this refers to the difference between an ellipsoid and a real aircraft fuselage, making it all the more important to verify their method and conclusions on a real aircraft model. Unfortunately, we found that some improvements must be made after attempting to apply it to an unmanned aerial vehicle (UAV).

As the extension of Da et al. [9], this paper aims to study the electric field computation method for real aircraft to further understand the problems caused by corona emissions.

II. Numeric Computation Method

A. Previous Method

One can solve Laplace's equation for the electric potential in three dimensions. From this solution, one can obtain the electric field vector $\boldsymbol{E}$ at any point from the gradient of electric potential. Rather than solve Laplace's equation as a differential equation by finite differences or finite elements, it is more convenient to solve the equivalent integral-equation form of Laplace's equation instead. The method of moments is such an integral method. In the aircraft body frame $\mathbf{O}$, mesh the surface to obtain n patches. Let the centroid and area of the ith patch be $\boldsymbol{r}_i = [x_i\ y_i\ z_i]^T$ and let S_i and the patch charge distribution σ_i be constant. Assuming the boundary condition of the equipotent potential, n potential equations can be established based on the method of moments as

$$\sum_{j=1}^{n} \int_{s_j} \frac{\sigma_j ds}{4\pi\varepsilon_0 |\boldsymbol{r}_i - \boldsymbol{r}|} + V_{i,\mathrm{EXT}} = U, \qquad V_{i,\mathrm{EXT}} = V_0 - \boldsymbol{r}_i \cdot \boldsymbol{E}_{\mathrm{ambient}} \tag{1}$$

Equation (1) denotes the potential equation in $\boldsymbol{r}_i$ and $i = 1{:}n$. In the left-hand side of Eq. (1), $V_{i,\mathrm{EXT}}$ is the potential due to the ambient electric field, V_0 is the potential of origin also due to the ambient electric field, and $\boldsymbol{E}_{\mathrm{ambient}} = [E_x\ E_y\ E_z]^T$ is the ambient electric field in the body frame, which is uniform around the aircraft. In the right-hand side of Eq. (1), U is the potential due to the net charge and the ambient electric field. If the body total net charge is Q, we can obtain the $(n+1)$th equation as

$$\sum_{i=1}^{n} S_i \sigma_i = Q \tag{2}$$

Combining Eq. (1) and (2) into the form of matrix results in

Received 22 May 2008; revision received 4 August 2008; accepted for publication 4 August 2008.

*Postgraduate, Postgraduate College; Dxingya@163.com.
†Professor, Department of Aeronautics; Shenhuair@tom.com.
‡Postgraduate, Postgraduate College; Redleilei@163.com.

$$\boldsymbol{A}\,[\,\sigma_1 \quad \sigma_2 \quad \cdots \quad \sigma_n \quad U - V_0\,]^T = \boldsymbol{B}\begin{bmatrix} E_x \\ E_y \\ E_z \\ Q \end{bmatrix}$$

where

$$\begin{aligned} \boldsymbol{A} &= \begin{bmatrix} \boldsymbol{P}_{n\times n} & -1_{n\times 1} \\ \boldsymbol{F}_{1\times n} & 0 \end{bmatrix}, \qquad \boldsymbol{P}_{ij} = \int_{s_j} \frac{ds}{4\pi\varepsilon_0 |\boldsymbol{r} - \boldsymbol{r}_i|} \\ \boldsymbol{F}_{1j} &= \int_{s_j} ds = S_j, \qquad \boldsymbol{B} = \begin{bmatrix} \boldsymbol{R}_{n\times 3} & 0_{n\times 1} \\ 0_{1\times 3} & 1 \end{bmatrix} \\ \boldsymbol{R} &= \begin{bmatrix} x_1 & y_1 & z_1 \\ x_2 & y_2 & z_2 \\ \cdots & \cdots & \cdots \\ x_n & y_n & z_n \end{bmatrix} \end{aligned} \tag{3}$$

For the arbitrary point $\boldsymbol{r}^*$ in which we are interested, the electric field can be expressed as

$$\begin{aligned} \boldsymbol{E}_{\boldsymbol{r}^*} &= \sum_{i=1}^{n} \sigma_i \int_{s_i} \frac{(\boldsymbol{r}^* - \boldsymbol{r})ds}{4\pi\varepsilon_0 |\boldsymbol{r}^* - \boldsymbol{r}|^3} + \boldsymbol{E}_{\text{ambient}} \\ &= \boldsymbol{D}_{3\times n}\begin{bmatrix} \sigma_1 \\ \sigma_2 \\ \vdots \\ \sigma_n \end{bmatrix} + \boldsymbol{E}_{\text{ambient}} \end{aligned} \tag{4}$$

where

$$\boldsymbol{D}_{\bullet j} = \int_{s_j} \frac{(\boldsymbol{r}^* - \boldsymbol{r})ds}{4\pi\varepsilon_0 |\boldsymbol{r}^* - \boldsymbol{r}|^3}$$

Substituting Eq. (3) into Eq. (4), the electric field at $\boldsymbol{r}^*$ becomes

$$\begin{aligned} \boldsymbol{E}_{\boldsymbol{r}^*} &= \begin{bmatrix} \boldsymbol{D} & 0_{3\times 1} \end{bmatrix} \boldsymbol{A}^{-1}\boldsymbol{B}\begin{bmatrix} E_x \\ E_y \\ E_z \\ Q \end{bmatrix} + \begin{bmatrix} \boldsymbol{I}_{3\times 3} & 0_{n\times 1} \end{bmatrix}\begin{bmatrix} E_x \\ E_y \\ E_z \\ Q \end{bmatrix} \\ &= \boldsymbol{C}_{3\times 4}\begin{bmatrix} E_x & E_y & E_z & Q \end{bmatrix}^T \end{aligned} \tag{5}$$

where

$$\boldsymbol{C} = \begin{bmatrix} \boldsymbol{D} & 0_{3\times 1} \end{bmatrix} \boldsymbol{A}^{-1}\boldsymbol{B}\begin{bmatrix} \boldsymbol{I}_{3\times 3} & 0_{3\times 1} \end{bmatrix}$$

To obtain an arbitrary point, $\boldsymbol{C}$ becomes a fixed 3×4 matrix. Once $[E_x\ E_y\ E_z\ Q]^T$ are given, the fields can be evaluated easily.

Equation (5) presents the basic model to compute the electric fields around an aircraft. To better evaluate $\boldsymbol{C}$ in our previous method, we used the symmetry of the aircraft that we found to decrease a half-patch; doing so improved computation precision. However, as the derivation is lengthy, we chose to present only the computation flow. More details can be found in [9]. The flow is as follows:

1) Mesh the left side of the aircraft and obtain left patches. Given that the patches on the right side are symmetrical with those on the left and that this method only needs to compute the left-side charge density, just one side needs to be meshed.

2) Compute the centroid coordinate $\boldsymbol{r}_i = [x_i\ y_i\ z_i]^T$ and area S_i of each left-side patch. The relationships between the left and corresponding symmetrical right patch are $\boldsymbol{r}'_i = [x_i\ -y_i\ z_i]^T$ and $S'_i = S_i$.

3) Compute potential matrix $\boldsymbol{A}_1$ when E_x, E_z, and Q are activated separately using

$$\boldsymbol{A}_1 = \begin{bmatrix} \boldsymbol{P}_{n\times n} & -1_{n\times 1} \\ \boldsymbol{F}_{1\times n} & 0 \end{bmatrix}, \quad \boldsymbol{F}_{1j} = \int_{s_j} \mathrm{d}s = S_j, \quad \boldsymbol{P}_{ij} = \int_{s_j} \frac{ds}{4\pi\varepsilon_0 |\boldsymbol{r}' - \boldsymbol{r}_i|}$$

where ε_0 is the vacuum permittivity.

4) Compute potential matrix $\boldsymbol{A}_2$ when E_y is activated using

$$\boldsymbol{A}_2 = \boldsymbol{P}_{n\times n}, \qquad \boldsymbol{P}_{ij} = \int_{s_j} \frac{ds}{4\pi\varepsilon_0 |\boldsymbol{r} - \boldsymbol{r}_i|} - \int_{s'_j} \frac{ds}{4\pi\varepsilon_0 |\boldsymbol{r}' - \boldsymbol{r}_i|}$$

5) Compute vector $\boldsymbol{B}_i (i = 1{:}4)$ using

$$\boldsymbol{B}_1 = \begin{bmatrix} x_1 \\ x_2 \\ \vdots \\ x_n \\ 0 \end{bmatrix}, \quad \boldsymbol{B}_2 = \begin{bmatrix} y_1 \\ y_2 \\ \vdots \\ y_n \end{bmatrix}, \quad \boldsymbol{B}_3 = \begin{bmatrix} z_1 \\ z_2 \\ \vdots \\ z_n \\ 0 \end{bmatrix}, \quad \boldsymbol{B}_4 = \begin{bmatrix} 0_{n\times 1} \\ 0.5 \end{bmatrix}$$

6) Solve equations $\boldsymbol{A}_1\boldsymbol{X}_1 = \boldsymbol{B}_1$, $\boldsymbol{A}_1\boldsymbol{X}_3 = \boldsymbol{B}_3$, $\boldsymbol{A}_1\boldsymbol{X}_4 = \boldsymbol{B}_4$, and $\boldsymbol{A}_2\boldsymbol{X}_2 = \boldsymbol{B}_2$ with the generalized minimal residual (GMRES) algorithm (see details in [10]), and obtain the results for $\widehat{x}_1$, $\widehat{x}_2$, $\widehat{x}_3$, and $\widehat{x}_4$

7) Given the coordinate $\boldsymbol{r}^*$ of the corona point or other points in which we are interested, evaluate $\boldsymbol{C}_i$ using

$$\begin{aligned} \boldsymbol{C}_1 &= \begin{bmatrix} \boldsymbol{D} + \boldsymbol{D}' & 0_{3\times 1} \end{bmatrix}\widehat{\boldsymbol{X}}_1 + \begin{bmatrix} 1 & 0 & 0 \end{bmatrix}^T \\ \boldsymbol{C}_2 &= (\boldsymbol{D} - \boldsymbol{D}')\widehat{\boldsymbol{X}}_2 + \begin{bmatrix} 0 & 1 & 0 \end{bmatrix}^T \\ \boldsymbol{C}_3 &= \begin{bmatrix} \boldsymbol{D} + \boldsymbol{D}' & 0_{3\times 1} \end{bmatrix}\widehat{\boldsymbol{X}}_3 + \begin{bmatrix} 0 & 0 & 1 \end{bmatrix}^T \\ \boldsymbol{C}_4 &= \begin{bmatrix} \boldsymbol{D} + \boldsymbol{D}' & 0_{3\times 1} \end{bmatrix}\widehat{\boldsymbol{X}}_4 \end{aligned}$$

$$\boldsymbol{D}_{\bullet j} = \int_{s_j} \frac{(\boldsymbol{r}^* - \boldsymbol{r})ds}{4\pi\varepsilon_0 |\boldsymbol{r}^* - \boldsymbol{r}|^3} (j = 1{:}n), \qquad \boldsymbol{D}'_{\bullet j} = \int_{s'_j} \frac{(\boldsymbol{r}^* - \boldsymbol{r})ds}{4\pi\varepsilon_0 |\boldsymbol{r}^* - \boldsymbol{r}|^3}$$

8) Compute the distorted electric field $\boldsymbol{E}_{\boldsymbol{r}^*}$ using

$$\begin{aligned} \boldsymbol{E}_{\boldsymbol{r}^*} &= \begin{bmatrix} \boldsymbol{C}_1 & \boldsymbol{C}_2 & \boldsymbol{C}_3 & \boldsymbol{C}_4 \end{bmatrix}\begin{bmatrix} E_x \\ E_y \\ E_z \\ Q \end{bmatrix} \\ &= \boldsymbol{C}_1 E_x + \boldsymbol{C}_2 E_y + \boldsymbol{C}_3 E_z + \boldsymbol{C}_4 Q \end{aligned}$$

9) Repeat steps 7 and 8 for the other points in which we are interested.

One advantage of this method is the visual and convenient form of its electric field computation model. Moreover, it needs just one linear system solution in step 6, making the computation more efficient when given different $[E_x\ E_y\ E_z\ Q]^T$.

B. New Method

We chose a UAV called TF-1 (Teng Fei 1), which has a wingspan of 3.1418 m used in atmospheric meteorological exploration, to verify our method and analyze the corona trigger factor. Its engine is located behind the fuselage and is in front of the upside-down V tail. We established the 3-D model without the engine using CATIA software and meshed the left-half surface to the 4241 patches using GAMBIT software. To decrease the number of patches, those on small curvature surfaces were meshed into quadrangles, with areas varying with the curvature. To guarantee a precise computation at the wing tip with a significant surface curvature, the patches in its vicinity were meshed into triangles with a length of less than 1 mm. The 3-D model and the meshing results are presented in Figs. 1 and 2. We discovered two problems from the previous method as we applied it to compute the fields around TF-1. We demonstrate the two problems and present our new solutions in the next section.

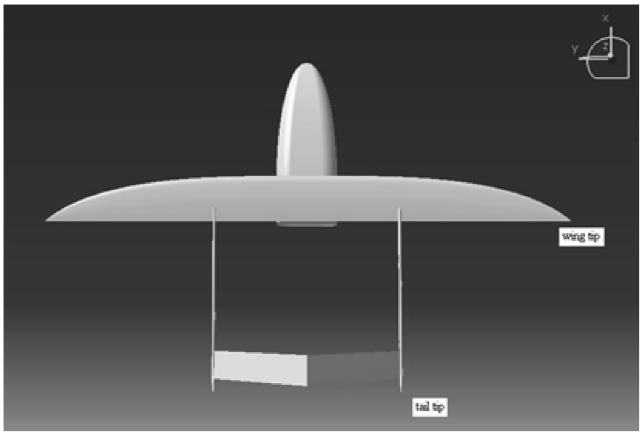

Fig. 1 TF-1 3-D model without the engine.

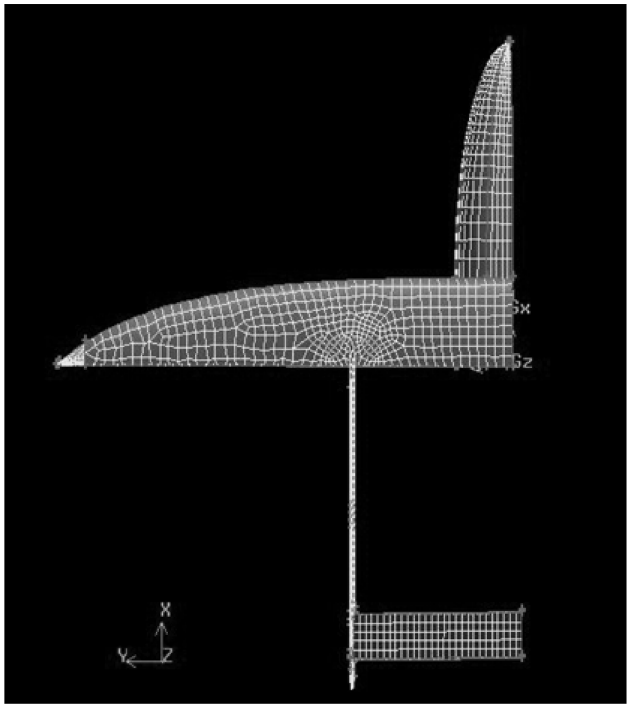

Fig. 2 Left-side surface patches of the TF-1.

When computing for the potential matrix in steps 3 and 4, the integral equations are singular if $i = j$: that is, when computing for the potential of the centroid of the ith patch due to the patch itself. To solve this problem, the previous method substitutes it with an equal-area circle patch. Generally, this method is suitable for a patch for which the aspect ratio is not too large or too small and for a quadrangle that can be subjected to specified maximum aspect ratios using special meshing software. However, if we restrict the aspect ratios, the patch number increases. Thus, it is better to solve the singular problem through analytical resolutions to improve precision as well as to simplify the meshing work. In the new method, we do not use such substitute technology any more because many quadrangle patches have very large aspect ratios that can cause great errors. Instead, we derived the analytical resolution (refer to Appendix A for the derivation).

After establishing the potential matrices, we found their condition numbers to be bigger than $1e6$. If we still use the GMRES algorithm to complete step 6, the computation will become almost stagnant. Therefore, we propose a new method here to complete step 6.

6-1) Evaluate $\boldsymbol{A}$'s eigenvalue vector λ and matrix $\boldsymbol{T}$, for which the columns are the corresponding eigenvectors. The relationship of the three matrices is $\boldsymbol{T}^{-1}\boldsymbol{A}\boldsymbol{T} = \mathrm{diag}(\lambda)$, where $\mathrm{diag}(\lambda)$ is the diagonal matrix of λ. Furthermore, we have $\boldsymbol{T}^{-1} = \boldsymbol{T}^T$ for the matrix $\boldsymbol{A}$ evaluated in our new method.

6-2) Compute $\boldsymbol{x}$ using $\boldsymbol{x} = \mathrm{diag}(\lambda)^{-1}\boldsymbol{T}^T\boldsymbol{B}$.

6-3) Compute $\boldsymbol{X}_0$ using $\boldsymbol{X}_0 = \boldsymbol{T}\boldsymbol{x}$.

6-4) If necessary, solve $\boldsymbol{A}\boldsymbol{X} = \boldsymbol{B}$ using the GMRES with the initial guess $\boldsymbol{X}_0$.

This new method is similar to precondition technologies, but much simpler to understand and use. In the next section we will make simulations to verify our new method.

III. Simulation

A. Computation Results

We selected the eigenfunction in MATLAB 6.5 that calls subroutines using the Arnoldi methods in ARPACK to evaluate λ and $\boldsymbol{T}$ in step 6-1. The time spent on the eigenfunction, using a computer with an AMD 3000 with a 1.8 GHz processor and 1.87 GB memory, was less than 20 min. We found that the residual error $\|\boldsymbol{r}\| = \|\boldsymbol{A}\boldsymbol{X}_0 - \boldsymbol{B}\|$ is less than $1e$-12. This showed that $\boldsymbol{X}_0$ is a good estimate of $\boldsymbol{A}\boldsymbol{X} = \boldsymbol{B}$ and step 6-4 could be omitted. If the residual error $\|\boldsymbol{r}\| = \|\boldsymbol{A}\boldsymbol{X}_0 - \boldsymbol{B}\|$ did not satisfy the precision requirement, step 6-4 could be called. Thus, the total time spent in our new step 6 was only about 20 min. This amount of time signifies a much more efficient system than with the previous stagnated GMRES method. The simulation results showed that our new method could guarantee speed and precision.

When steps 1 to 6 are completed using our preceding new method, we can then evaluate the distorted electric field at arbitrary points. With only the wing-tip and tail-tip fields presented in the corona analysis, given the coordinates of $\boldsymbol{r}_{\text{wing tip}} = [0, 1.7088, 0.2]^T$ and $\boldsymbol{r}_{\text{tail tip}} = [-1.1, 0.6, 0.21]^T$, the computation results are

$$\boldsymbol{C}_{\text{wing tip}} = \begin{bmatrix} -1.08 & -193.54 & 0.24 & -107.31/4\pi\varepsilon_0 \\ 5.74 & 601.46 & -0.78 & 333.23/4\pi\varepsilon_0 \\ 0.01 & 1.40 & 0.96 & 0.76/4\pi\varepsilon_0 \end{bmatrix}$$

and

$$\boldsymbol{C}_{\text{tail tip}} = \begin{bmatrix} 154.49 & -84.96 & 10.35 & -118.50/4\pi\varepsilon_0 \\ -1.10 & 0.66 & -0.08 & 0.86/4\pi\varepsilon_0 \\ -1.80 & 0.97 & -0.06 & 1.37/4\pi\varepsilon_0 \end{bmatrix}$$

B. Results Analysis

The matrix $\boldsymbol{C}_{\text{wing tip}}$ is mainly determined by E_y and Q, as already noted. It shows us that the wing-tip field mainly contains x and y components in the aircraft body frame and that the z component is almost zero, compared with the other two. Figure 3a shows the wing-tip shape. As can be seen, the two lines represent the tangent lines of the two edges at the tip, where one is a line and the other is a curve. The sharp shape and the two tangent lines determine the field direction at the tip, which should lie in the angle between the two tangent lines, which is about 38 deg. In our result, the angle between the wing-tip field direction and the positive y axis is about 17.8 deg, which is within the angle of two tangent lines.

The normal line of the tail tip is parallel with the x axis, which indicates that the tail-tip field direction must be toward the x axis. It also means that the elements in rows 2 and 3 of $\boldsymbol{C}_{\text{tail tip}}$ should all be zeros. These elements are not zeros in our result, but are rather small compared with row 1.

Although we cannot derive theoretical values at both the wing tip and the tail tip, the insignificant differences of the field directions between the theories and our computation results still indicate that our results are reasonable and the errors in the fields are small.

C. Real Aircraft Corona Trigger-Factor Analysis

If we neglect the small components due to E_x and E_z at the wing tip, as well as the y and z components at the tail tip, the tip fields can be expressed as

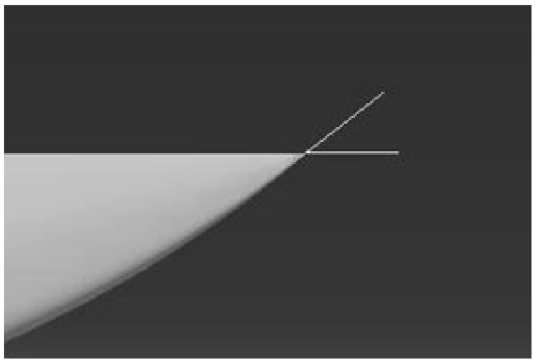

a)

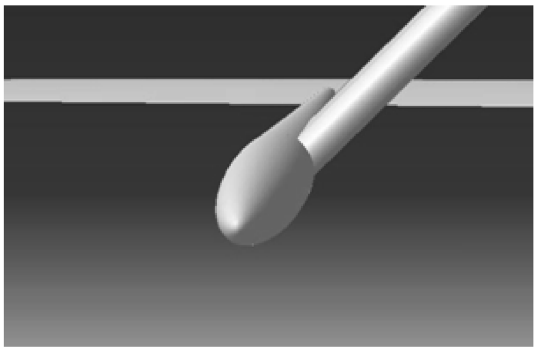

b)

Fig. 3 Shapes of the a) wing tip and b) tail tip.

$$E_{\text{wing tip}} = \begin{bmatrix} -193.54E_y - 107.31Q/4\pi\varepsilon_0 \\ 601.46E_y + 333.23Q/4\pi\varepsilon_0 \\ 0 \end{bmatrix}$$

and

$$E_{\text{tail tip}} = \begin{bmatrix} 154.49E_x - 84.95E_y + 10.34E_z - 118.50Q/4\pi\varepsilon_0 \\ 0 \\ 0 \end{bmatrix}$$

By analyzing the wing-tip field, we find that when

$$Q\sqrt{333.23^2 + 107.31^2/4\pi\varepsilon_0} > E_y\sqrt{601.46^2 + 193.54^2}$$

(that is, $Q/E_y > 1.81 \times 4\pi\varepsilon_0 \approx 0.2\ \mu\text{C}\cdot\text{m}\cdot\text{kV}^{-1}$),[§] the contribution due to Q exceeds that of E_y, and the aircraft net charge becomes the main corona trigger factor. Many studies have shown that while penetrating clouds, especially storms, the E_x and E_y components will run up to 20 kV/m, and the aircraft net charge will run up to hundreds of microcoulombs [11]. If E_y is 20 kV/m, the net charge will be the main trigger factor when it exceeds 4 μC. Such a strong field component is an extreme situation that always appears in clouds and storms or near storms in which the density of the particles charging the aircraft through collisions is larger. If such situations occur, the aircraft net charge will also run up to an extremely high level (far more than 4 μC). When the ambient field is not strong enough to trigger wing-tip corona emissions, the net charge inevitably becomes the trigger factor once corona emissions occur. More details about the relationship between aircraft charging and ambient field can be found in [11,12].

A similar analysis can be made for the tail tip. We find that when

$$118.5021Q/4\pi\varepsilon_0 > 10.3467E_z, \qquad 118.5021Q/4\pi\varepsilon_0 > 84.9554E_y$$
$$118.5021Q/4\pi\varepsilon_0 > 154.4942E_x$$

that is,

$$Q/E_x > 0.145\ \mu\text{C}\cdot\text{m}\cdot\text{kV}^{-1}, \qquad Q/E_y > 0.08\ \mu\text{C}\cdot\text{m}\cdot\text{kV}^{-1}$$
$$Q/E_z > 0.0097\ \mu\text{C}\cdot\text{m}\cdot\text{kV}^{-1}$$

the net charge becomes the main factor. Under an extreme situation in $E_z = 1000$ kV/m, $E_x = 20$ kV/m, and $E_y = 20$ kV/m, the net charge requires only 9.7 μC to become the main factor, which is also a rather low level in such a situation. Indeed, the E_z component rarely exceeds 200 kV/m in the clouds.

D. Other Aircraft

We only discussed the corona trigger factor specifically for the TF-1. However, this analysis method can also be applied to other aircraft. Lacking real aircraft models, we were not able to expand the conclusion of the net charge being the main corona trigger factor in this paper. However, it is evident that the conclusion would also be correct for other aircraft.

E. Corona Prediction

If the distorted field expression is evaluated and the ambient field and net charge are measured, one could predict where and when corona emissions would occur. It seems impossible to measure the ambient field and net charge while flying. However, if an aircraft has been installed no less than four electric field meters, such as in the case of an atmospheric field measurement aircraft, the four unknowns can be measured. Thus, we may solve the foundational corona-prediction problem for field measurement aircraft, which is also the aim of our work. The following is our prediction scheme for a field measurement aircraft:

1) Obtain the distorted field expression using the new method presented in this paper at any point at which a corona may be triggered.

2) Measure the ambient field and the net charge on the surface using the linear field measurement theory (see [13] for related details).

3) Evaluate the distorted field at all possible points using the data obtained in the previous step.

4) Predict corona emissions at any point by comparing the distorted field with the corona threshold field strength.

5) If a corona exists, correct the measurements to improve precision.

Arriving at the solution in the fifth step will be our next main topic.

IV. Conclusions

In this paper, we mainly improved the previous field computation method using analytical resolutions of potential matrix elements and by proposing a simple linear system solution technology. The simulation shows that these improvements are successful. We find that the aircraft net charge is a main corona trigger factor regardless of whether it flies in strong field areas. These successful findings provide us a scheme with which to predict corona emissions for field measurement aircraft. In addition, if the corona threshold field is 2600 kV/m, we find an extreme situation that a total net charge of only 0.83 μC[¶] on the TF-1 will trigger corona emissions even if the ambient field is zero. This could heavily endanger the communication system of the TF-1 in atmospheric explorations as it penetrates storms and clouds. Thus, the problems caused by corona emissions in the TF-1 need to be seriously solved.

[§]The errors of $\boldsymbol{C}$ are caused by two parts: one is the surface meshing error, which is due to the difference between a real aircraft and its 3-D meshes, and the other is the numeric computation error. Although $\boldsymbol{C}_i$ is evaluated separately, we still used the same meshes. Therefore, the errors caused by the 3-D modeling difference are the same. Meanwhile, the computation errors are almost the same, which are judged by the almost equal residual errors in step 6. We believe the relative errors of elements of $\boldsymbol{C}$ are almost close. This indicates that the error of $C_{ij}/C_{ik}(j \neq k)$ is smaller no matter how large the relative error of $\boldsymbol{C}$ is. It is our opinion that 0.2 $\mu\text{C}\cdot\text{m}\cdot\text{kV}^{-1}$ is precise, and the same conclusion likewise suits the evaluated ratio.

[¶]The numeric value is evaluated at the wing tip when the ambient field is zero.

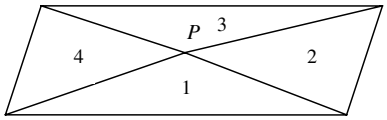

a)

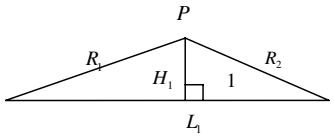

b)

Fig. A1 Illustrations of a) segments of a quadrangle patch and b) length definition of segment 1.

Appendix A: Parameter Computation

If the integral is not singular, we substitute the face charge with a point charge and come up with

$$\boldsymbol{D}_{\bullet j} = \frac{(\boldsymbol{r}^* - \boldsymbol{r}_j)S_j}{4\pi\varepsilon_0|\boldsymbol{r}^* - \boldsymbol{r}_j|^3}, \qquad \int_{s_j} \frac{ds}{4\pi\varepsilon_0|\boldsymbol{r} - \boldsymbol{r}_i|} = \frac{S_j}{4\pi\varepsilon_0|\boldsymbol{r}_i - \boldsymbol{r}_j|}$$

$$\boldsymbol{D}'_{\bullet j} = \frac{(\boldsymbol{r}^* - \boldsymbol{r})S_j}{4\pi\varepsilon_0|\boldsymbol{r}^* - \boldsymbol{r}'_j|^3}, \qquad \int_{s'_j} \frac{ds}{4\pi\varepsilon_0|\boldsymbol{r}' - \boldsymbol{r}_i|} = \frac{S_j}{4\pi\varepsilon_0|\boldsymbol{r}_i - \boldsymbol{r}'_j|}$$

If the integral is singular (that is, when computing for the potential of the centroid P of a patch due to the patch itself), we deduce an analytical resolution. We segment the patch into four parts and label them as 1, 2, 3, and 4, as shown in Fig. A1. As the derivation is lengthy, only the results are subsequently given.

The potential at P is the sum of four contributions from each of the four segments. In segment 1, the length of the three edges are R_1, R_2, and L_1, and the height is H_1. We can compute the potential due to segment 1 through this expression:

$$\Delta U_1 = \frac{\sigma H_1}{4\pi\varepsilon_0}\ell_n\frac{L_1^2 + 2R_2L_1 - R_1^2 + R_2^2}{2R_1L_1 - R_1^2 - L_1^2 + R_2^2},$$

$$H_1 = R_1\sqrt{1 - \left(\frac{R_1^2 + L_1^2 - R_2^2}{2R_1L_1}\right)^2}$$

where σ is the patch's unknown charge density. The potential at P due to the patch charge is the sum of $\Delta U_i (i = 1{:}4)$. Therefore, the potential matrix element can be evaluated using

$$\int_{s_i} \frac{ds}{4\pi\varepsilon_0|\boldsymbol{r} - \boldsymbol{r}_i|} = \frac{\Delta U_1 + \Delta U_2 + \Delta U_3 + \Delta U_4}{\sigma}$$

Note that this procedure represents a face-integral formulation and that this algorithm is valid for triangle patches.

References

[1] Jones, J. J., Winn, W. P., and Han, F., "Electric Field Measurements with an Airplane: Problems Caused by Emitted Charge," *Journal of Geophysical Research*, Vol. 98, No. D3, 1993, pp. 5235–5244. doi:10.1029/92JD02686

[2] Mo, Q., Ebneter, E., Fleischhacker, P., and Winn, W. P., "Electric Field Measurements with an Airplane: A Solution to Problems Caused by Emitted Charge," *Journal of Geophysical Research*, Vol. 103, No. D14, 1998, pp. 17163–17173. doi:10.1029/98JD01149

[3] Mo, Q., Feind, R. E., Kopp, F. J., and Detwiler, A. G., "Improved Electric Field Measurements with the T-28 Armored Research Airplane," *Journal of Geophysical Research*, Vol. 104, No. D20, 1999, pp. 24485–24497. doi:10.1029/1999JD900834

[4] Rudolph, T. H., Perala, R. A., "Interpretation Methodology and Analysis of In-Flight Lightning Data," NASA CR-3590, 1982.

[5] Mazur, V., Ruhnke, L. H., Rudolph, T., "Effect of E-Field Mill Location on Accuracy of Electric Field Measurements with Instrumented Airplane," *Journal of Geophysical Research*, Vol. 92, No. D10, 1987, pp. 12013–12019. doi:10.1029/JD092iD10p12013

[6] Stathopulos, I. A., "Three-Electrode System on DC Electric Field," 3rd International Symposium on High Voltage Engineering, Milan, Italy, National Societies of Electrical Engineers of Europe, Paper 12.03, 1979.

[7] Parker, L. W., and Kasemir, H. W., "Predicted Aircraft Field Concentration factors and Their Relation to Triggered Lightning," International Aerospace and Ground Conference on Lightning and Static Electricity, National Interagency Coordination Group Paper 9, June 1984.

[8] Yi, M., Wang, C., "Investigation on Electrostatic Charge Distribution and Landing Discharge of Fixed Wing Aircraft," *High Voltage Engineering*, Vol. 33, No. 7, 2007, pp. 115–118.

[9] Da, X., Hong, L., and Shen, H., "Computation Model of Electric Field Around Aircraft Penetrating Clouds," 7th International Conference on System Simulation and Scientific Computing, Beijing, Beijing Univ. of Aeronautics and Astronautics, Paper 21, 2008.

[10] Saad, Y., and Schultz, M. H., "GMRES: A Generalized Minimal Residual Algorithm for Solving Nonsymmetric Linear Systems," *SIAM Journal on Scientific and Statistical Computing*, Vol. 7, No. 3, 1986, pp. 856-869.

[11] Jones, J. J., "Electric Charge Acquired by Airplanes Penetrating Thunderstorms," *Journal of Geophysical Research*, Vol. 95, No. D10, 1990, pp. 16589–16600. doi:10.1029/JD095iD10p16589

[12] Illingworth, A. J., and Marsh, S. J., "Static Charging of Aircraft by Collisions with Ice Crystals," *Revue de Physique Appliquée*, Vol. 21, Dec. 1986, pp. 803–808.

[13] Koshak, W. J., "Retrieving Storm Electric Fields from Aircraft Field Mill Data Part 1: Theory," *Journal of Atmospheric and Oceanic Technology*, Vol. 23, Oct. 2006, pp. 1289–1302. doi:10.1175/JTECH1917.1